



**HAL**  
open science

## Interface microstructure formation of dissimilar Fe/Fe–Mn–C steel RSW joints

Julien Zollinger, M. Escot, L. Deillon, B. Rouat, D. Daloz, T. Dupuy

► **To cite this version:**

Julien Zollinger, M. Escot, L. Deillon, B. Rouat, D. Daloz, et al.. Interface microstructure formation of dissimilar Fe/Fe–Mn–C steel RSW joints. *Journal of Materials Processing Technology*, 2018, 252, pp.697-704. 10.1016/j.jmatprotec.2017.10.031 . hal-02353577

**HAL Id: hal-02353577**

**<https://hal.univ-lorraine.fr/hal-02353577>**

Submitted on 7 Nov 2019

**HAL** is a multi-disciplinary open access archive for the deposit and dissemination of scientific research documents, whether they are published or not. The documents may come from teaching and research institutions in France or abroad, or from public or private research centers.

L'archive ouverte pluridisciplinaire **HAL**, est destinée au dépôt et à la diffusion de documents scientifiques de niveau recherche, publiés ou non, émanant des établissements d'enseignement et de recherche français ou étrangers, des laboratoires publics ou privés.

# Interface microstructure formation of dissimilar Fe/Fe-Mn-C steel RSW joints

J. Zollinger<sup>a,b,\*</sup>, M. Escot<sup>†a,c</sup>, L. Deillon<sup>‡a</sup>, B. Rouat<sup>a,b</sup>, D. Daloz<sup>a,b</sup>, T. Dupuy<sup>c</sup>

<sup>a</sup>Université de Lorraine, Institut Jean Lamour, Department of Metallurgy & Materials Science and Engineering, Parc de Saurupt, F-54011 Nancy, France.

<sup>b</sup>Laboratory of Excellence on Design of Alloy Metals for low-mAss Structures ('LabEx DAMAS'), France

<sup>c</sup>ArcelorMittal R&D, Automot. prod., Voie Romaine, F-57283 Maizières-lès-Metz, France

---

## Abstract

An experiment was developed to simulate the interface between liquid high manganese carbon steel and solid ultra-low alloyed steel in a thermal gradient, corresponding to the nugget / sheet interface of resistance spot welds. Despite the large difference in the interaction time between the experiment and the welding process, identical microstructures and phases were observed in both. The time and temperature control of the experimental set-up indicates that the solute diffusion in the solid and liquid phase together with the interface temperature when cooling determines the microstructure formation and morphology. The presence of  $\epsilon$ -martensite requires a  $\gamma$  / liquid interface with a manganese-driven dissolution. A criterion based on manganese supersaturation is proposed and shows that with the studied steels the nucleation and growth of  $\epsilon$ -martensite is almost unavoidable when using resistance spot welding. The cellular patterns observed during solutal melting at low interface temperature increase the interface surface and the amount of martensite. The origin of the cells is the carbon enrichment in the manganese diffusion zone of the  $\gamma$  phase that provokes a solidus temperature gradient in the thermal gradient.

**Keywords:** Microstructures, Interfaces, Solutal melting, Resistance spot welding, Mn steels

---

## 1. Introduction

Success of dissimilar welding is achieved when the welded zone is as resistant as the weaker of the dissimilar material. In order to reach this objective, dissimilar welding has to deal not only with rapid solidification and heat affected zone structural modification, but also with dilution, segregation and the possibility for new phases to nucleate that may weaken the joint. The most common process to join steels in the automotive industry is resistance spot welding (RSW). The process-structure-properties relationship in RSW have been addressed in a review by Pouranvari and Marashi [Pouranvari and Marashi \(2013\)](#). Among the different studies dedicated to dissimilar steel welding, Pouranvari *et al.* showed the importance of the dilution ratio to control the amount of martensite resulting from the resistance spot welding of AISI 304 austenitic stainless steel and AISI 1008 low carbon steel [Pouranvari and Marashi \(2011\)](#). Concerning the welding of TWIP steel with dual phase steel via laser beam, Rossini *et al.* suggests that Mn segregation was responsible for brittleness leading to inter-granular fracture [Rossini et al. \(2015\)](#). On the other hand, Mujica *et al.* showed in laser beam welding the formation of brittle martensitic bands when welding together TWIP and TRIP steel [Mujica et al. \(2010\)](#). In many cases where high manganese steels are to be joined with less alloyed steels, martensite close to the nugget / heat affected zone interface is often found to be a weakness of the weld [Rajinikanth et al. \(2013\)](#); [Russo Spina et al. \(2016\)](#).

In this work, the joining of dissimilar steels is investigated with an ultra-low alloyed (ULA) ferritic steel and a high-manganese (HM) austenitic steel. ULA steels are typical forming grades for car body and HM steels are advanced high strength steels for safety parts; successfully welding these steels is of obvious technological importance. Joint

---

<sup>†</sup>Present address: Aperam alloys, F-58160 Imphy, France

<sup>‡</sup>Present address: LMM, EPFL, CH-1015 Lausanne, Switzerland

\*Corresponding author: [julien.zollinger@univ-lorraine.fr](mailto:julien.zollinger@univ-lorraine.fr)

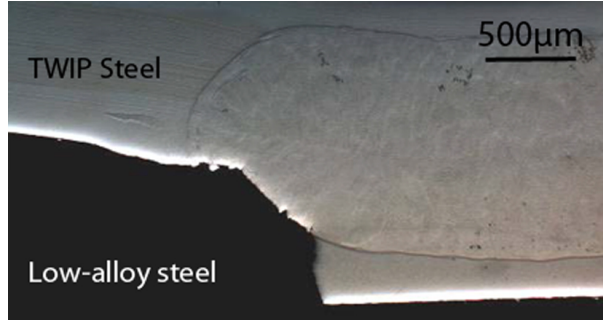


Figure 1: Fracture on a dissimilar steels sheets that were resistance spot welded. The fracture is located at the ULA steel/melted zone interface at the edge of the axis of current flow.

Alloy	Fe	Mn	C	P	S	Si	Other	$T_\ell$ (°C)
ULA	Bal.	0.22	0.0014	< 0.010	< 0.012	0.02	< 0.1	1538
High-Mn	Bal.	22	0.6	< 0.03	< 0.010	0.2	< 0.2	1425

Table 1: Composition (weight percents) and liquidus temperature of the steels used in this study.

of this type performed with RSW and mechanically tested show failure mainly at the edge of the melted zone / low alloyed steel interface, as shown in Figure 1. As can be seen from this figure, the melted zone is asymmetrical (due to different melting temperatures and thermal properties of the steels) and is larger on the HM steel side. At the microscopic scale, while the ULA remains fully ferritic, the HM steel and the melted zone are fully austenitic, the crack initiation occurs on small martensite colonies located again at the edge of the melted zone / low alloyed steel interface.

Different types of martensite can be observed in Fe-Mn-C steels depending mainly on the manganese concentration; the usual body-centered tetragonal martensite noted  $\alpha'$  is observed for Mn content lower than 10 wt.% whereas a hexagonal martensite noted  $\epsilon$  is favoured at higher Mn contents Schumann (1972). Since the composition in the melted zone is expected to be homogeneous because of the important stirring induced by the process Li et al. (2011), it is unclear why martensite colonies are located only at the edge of melted zone / ULA steel.

From the observations made from RSW failures between HM and ULA steels: (i) the area of interest is located at the melted zone / ULA steel interface; this zone corresponds to the end of the melting stage with a liquid / solid interface velocity,  $v^* \approx 0$  during the welding, (ii) the solid ULA steel, which is almost pure iron, is in contact with a liquid that is richer in both carbon and manganese; thus solute diffusion may play a role. A new lab-scale experimental set-up has been developed in order to investigate the behaviour of the solid ULA / Mn- and C-rich liquid interface in a thermal gradient. This novel approach is presented in the next section that details the experimental set-up; the main results are then shown and discussed.

## 2. Experimental Materials and procedure

The experimental set-up is described in Figure 2. The furnace consists of a hot zone, an induction-heated graphite susceptor and a cool zone, cooled with water. The samples are placed into an alumina crucible that is positioned in the furnace then sealed within a quartz enclosure allowing operation under vacuum or argon gas flow. The graphite susceptor is instrumented with two Pt/Pt-Rh thermocouples to control the temperature of the furnace at different heights. The ULA and HM steels (nominal composition and liquidus temperatures are given in Table 1) were cast at ArcelorMittal R&D into cylindrical bars with 5mm diameter and 200 mm length. The ULA steel cylinders were cut into 80 mm length and the HM steel cylinders were cut into 30 and 100 mm length samples.

For the present investigations, the hot zone was heated up to 1650°C under argon flow after a primary vacuum was established. The ULA steel was positioned in the bottom of the crucible while the HM steel was placed on top, with the initial interface position at 1500°C so that the HM steel is liquid and the ULA steel remains solid. The thermal gradient  $G_T^\ell$  in the liquid was measured with an alumina-sheathed Pt/Pt-Rh thermocouple to be 3000 K.m<sup>-1</sup> for the

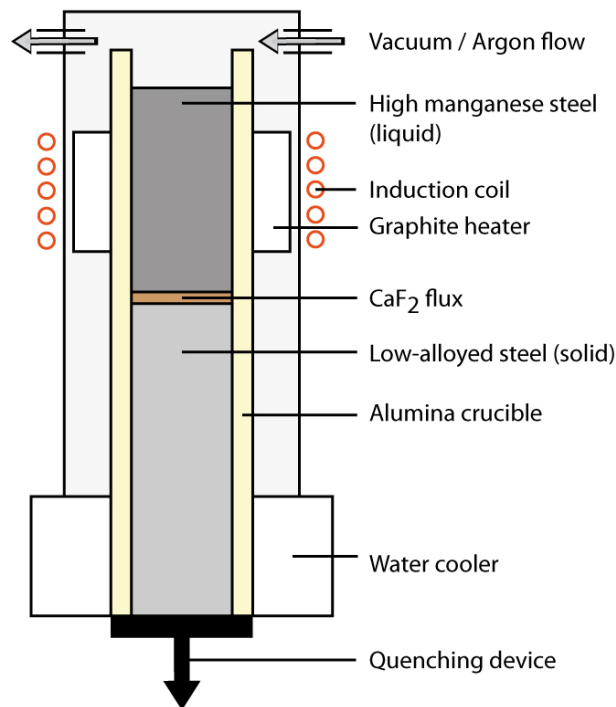


Figure 2: Schematic of the experimental set-up.

100 mm length HM samples and  $8000 \text{ K.m}^{-1}$  for the 30 mm HM samples. Before the experiments, the steel bars were polished with grit 1200 SiC paper and calcium fluoride flux was used to deoxidise the surfaces and ensure good contact between the two steels. Within this set-up, the only variable was the holding time: 0, 1, 3, 6 and 10 minute holds were performed for the 30 mm length samples and 0, 10, 20 and 30 minute holds were used for the 100 mm length samples; at the end of the experiment the interface was moved into the water cooler with a pneumatic jack, quenching the solid / liquid interface at a cooling rate of about  $200 \text{ K.s}^{-1}$ . Every experiment was performed twice in order to ensure the reproducibility of the results.

After standard metallographic preparation, the longitudinal sections of the samples were electrolytically polished with a LectroPol-5 apparatus and A1 solution from Struers for SEM examination or etched with a Béchét-Beaujard etchant for OM examination. Samples were examined by SEM and OM for imaging, energy dispersive spectroscopy (EDS) for chemical analysis, and electron backscatter diffraction (EBSD) for phase identification on a FEI Quanta 600 F FEG-SEM equipped with a Bruker Si-drift Quantax EDS detector and a Nordlys high speed EBSD camera. Electron-Probe Micro-Analysis (EPMA) was performed with a CAMECA SX100 electron probe microanalyzer; and calibration curves were determined to quantify carbon contents. Micro-hardness measurements were performed diagonally with respect to the interface using a Vickers indenter with a load of 100 g (HV 0.1). Indentation spacings were refined for RSW samples because the microstructures obtained in welding are much finer.

Thermodynamic calculations were performed using the ThermoCalc software [Andersson et al. \(2002\)](#) and the Fe-Mn-C database proposed by Djurovic *et al.* [Djurovic et al. \(2011\)](#) to determine liquidus and solidus temperatures, isothermal sections and peritectic temperatures.

### 3. Welding and experimental microstructures

Figure 3 shows the microstructures observed at the solid / liquid interface in samples from the experiments and in RSW. In these figures, the solidified liquid (HM steel) is located at the top of the micrographs (brown colored dendrites) whereas the solid ULA steel is at the bottom (light gray). Two types of interfaces were observed in both experiments and RSW joints. The first type of interface is planar (Figures 3(a) and (b)) e.g. a flat and regular

solid / liquid interface is observed. The second type of microstructure observed is presented in Figures 3(c) and (d) and consists of a cells-like array of dissolving ULA steel. The main difference between these two figures is the cellular spacing which is much smaller in the RSW specimen, because both the thermal gradient and the solid / liquid interaction time are one or more orders of magnitude greater and shorter, respectively, in RSW; which will be discussed in more detail in the next section. In these low magnification images,  $\epsilon$  martensite needles can be distinguished at the tip of the cells in Figures 3(c) and (d). These first observations validate the designed experiment and the assumptions discussed earlier, the low solid / liquid interface velocity and a solute diffusion controlled microstructure evolution.

Micro-hardness measurement were performed in order to determine if the quenching in the experiment resulted in a cooling rate leading to similar room-temperature (RT) microstructure and properties. The results are shown in Figure 4(a) for the experiments and in Figure 4(b) for the RSW specimens. Significant differences are observed between the micro-hardness profiles, but in both cases there is a peak of hardness in the samples where the interface microstructure is cellular. The difference between hardness maxima and hardness in ULA steel, as well as the spatial extent of the large hardness zones, can be explained by the joining method used.

The values of the hardness peak that differs from the experiment and the RSW specimen are due to the size of the microstructure as shown in Figure 3(c) and (d). The hardness indents in this area typically have a size of 20  $\mu\text{m}$  which is smaller than the cellular array in Figure 3(c) but larger than the one obtained in RSW and presented in Figure 3(d). In the latter case, the measured value is thus an average value between the ULA steel, the interface and the HM steel microstructures. The extent of the hard zone in the experiment and the difference in hardness in the ULA steel between the experiment and the RSW can be attributed to the different scale of the microstructure,

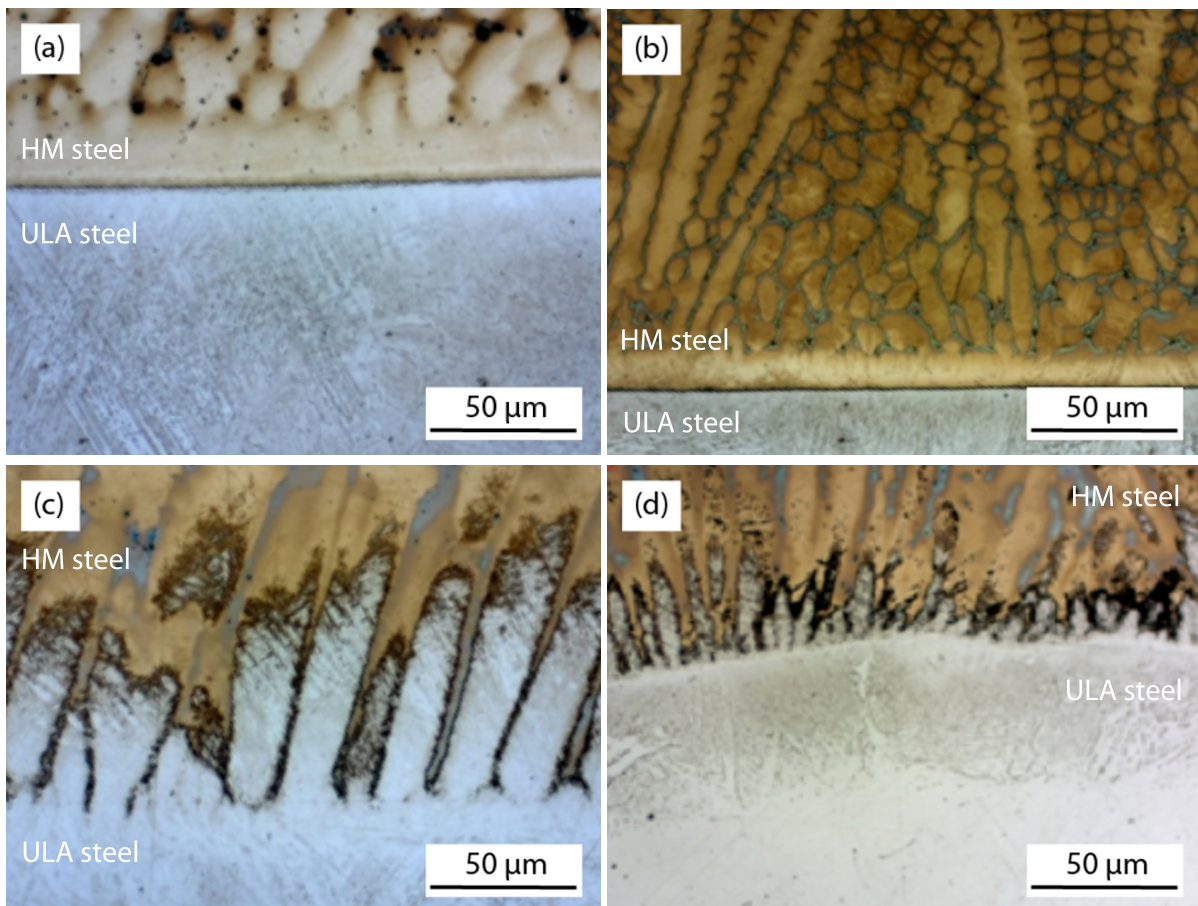


Figure 3: Comparison between the two types of microstructures observed in the samples (a)  $G_T^l = 8000 \text{ K/m}$ , 3 minutes holding and (c)  $G_T^l = 3000 \text{ K/m}$ , 20 minutes holding, and in resistance spot welded specimens (b) and (d).

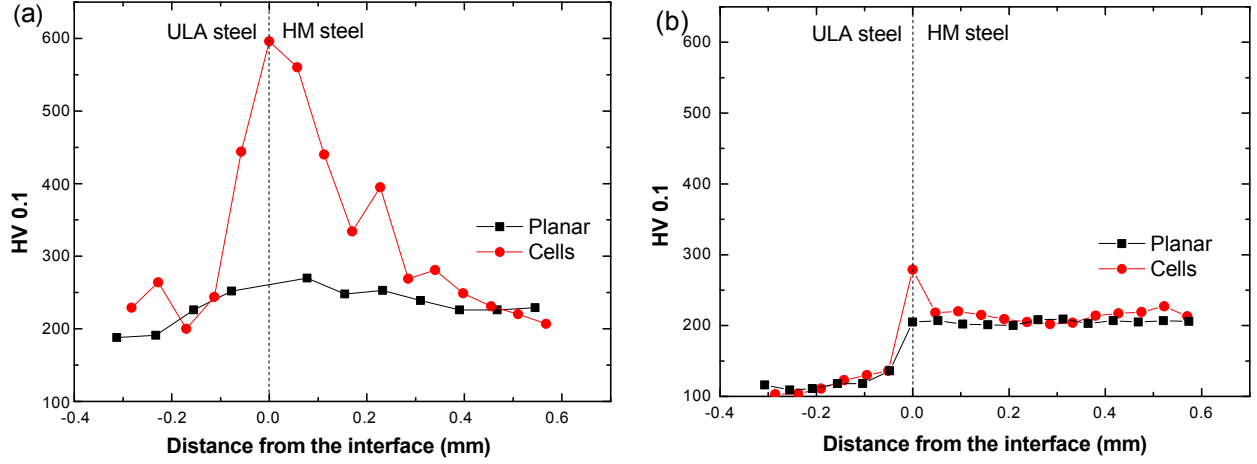


Figure 4: HV 0.1 micro-hardness measurements corresponding to the interfaces presented in (a) Figure 3(a) and (c); and (b) Figure 3(b) and (d).

but also to the extent of the diffusion and heat affected zones. The characteristic times between the two methods are very different: of the order of 0.1 seconds for the RSW and of several minutes for the experiments. Also, the thermal gradients differ significantly from  $3000-8000 \text{ K.m}^{-1}$  in the experiment to a value of approximately  $10^6 \text{ K.m}^{-1}$  in RSW (corresponding to the temperature difference between the copper electrode and the steel liquidus over the sheet thickness). This leads to very thin heat and diffusion affected zones in the RSW specimens at the interface, while in the experimental set-up these zones are much larger and explain the higher hardness measured in the ULA steel. The HM steel is cooled quickly from the liquid state in both joining methods, and Figure 4(b) and (c) show similar values of 210 to 220 HV.

The designed experiment is suitable to produce samples that exhibit similar microstructures to that observed in RSW specimens. The samples processed show identical morphologies and reproduce the change in mechanical properties observed at the interface in the case of welding. A deeper analysis of the interfacial microstructures obtained with the experimental set-up will now be presented with focus on the temperature and phases at the solid / liquid interface.

#### 4. Microstructure evolution

This section approaches the problem of a solute-driven moving interface of a ternary system in a thermal gradient, and its consequences on the interfacial microstructure of the dissimilar steels. A simple model to address solutal melting is given. The observed microstructures *vs.* interface temperature are then presented. Finally phase selection during dissolution and its morphology are discussed.

##### 4.1. Model for dissolution kinetics

The interface velocity  $v^*$  can be addressed by writing a solute balance at the interface for each solute using the following equation:

$$w_i^{\ell*} (1 - k_i^{\varphi/\ell}) v^* = G_i^\ell D_i^\ell - G_i^\varphi D_i^\varphi \quad (1)$$

where  $\ell$  denotes the liquid phase,  $\varphi = (\delta, \gamma)$ ,  $w_i^{\ell*}$  is the liquid weight fraction of  $i$  ( $i = \text{C, Mn}$ ) at the interface,  $k_i^{\varphi/\ell}$  is the partition coefficient between the solid and the liquid phases,  $v^*$  is the interface velocity,  $G_i$  are the chemical gradients and  $D_i$  the diffusion coefficients. The chemical gradients can be expressed as :

$$G_i^\ell = \frac{w_i^{\ell*} - w_i^{\ell\infty}}{\delta_\ell} \quad (2)$$

for the liquid phase and as

$$G_i^\varphi = \frac{w_i^{\varphi\infty} - w_i^{\varphi*}}{\delta_\varphi} \quad (3)$$

for the solid phase.  $\delta$  is a diffusion length that can be expressed versus time  $t$  as:

$$\delta = \sqrt{6 \cdot D_i \cdot t} \quad (4)$$

Incorporating Eq. 2-4 into Eq. 1 gives an expression of the interface velocity:

$$v^* = \frac{w_i^{\ell*} - w_i^{\ell\infty}}{w_i^{\ell*}(1 - k_i^{\varphi/\ell})} \cdot \sqrt{\frac{D_i^\ell}{6 \cdot t}} + \frac{w_i^{\varphi*} - w_i^{\varphi\infty}}{w_i^{\ell*}(1 - k_i^{\varphi/\ell})} \cdot \sqrt{\frac{D_i^\varphi}{6 \cdot t}} \quad (5)$$

Finally expressing the weight fraction ratios as supersaturations  $\Omega_i$ , the interface velocity reads:

$$v^* = \frac{1}{\sqrt{6 \cdot t}} \sum_{j=\ell, \varphi} \Omega_i^j \cdot \sqrt{D_i^j} \quad (6)$$

The supersaturations defined here are different than those usually encountered in solidification or melting of homogeneous alloys where they range from 0 to 1. Due to large chemical heterogeneities between the solid ULA and liquid HM steel, in the present work supersaturations can have maximum absolute values much larger than 1 and can be negative in the case of liquid phase, i.e.  $0 \geq |\Omega_i^j| \gg 1$ . Solving Eq. 6 requires determining the interfacial compositions through a flux balance for Mn and C. This can require the use of irreversible thermodynamics as described by Hillert [Hillert \(1999\)](#) or Lesoult [Lesoult \(2012\)](#), from the initial analysis by Baker and Cahn [Baker and Cahn \(1971\)](#), the interface properties such as interface diffusion coefficient  $D_i^*$  and interface thickness [Svoboda et al. \(2011\)](#). While these aspects are out of the scope of the present paper, an analysis based on non dimensional parameters can be performed and will be discussed in section 4.3.

#### 4.2. Influence of temperature on microstructure

The initial position of the interface was initially at 1500 °C. With diffusion of the alloying elements in the ULA steel, its liquidus temperature decreases leading to dissolution of the solid and a displacement of the interface in the thermal gradient at lower temperature. Knowing the thermal gradient at the interface, quenching the interface after different holding time allows associating of an interface temperature to the corresponding microstructure.

Figure 5(a) and (b) show the two types of microstructures discussed in the previous section with SEM-BSE images. Figure 5(a) shows a planar interface obtained with a 10 min. holding and  $G_T^\ell = 3000$  K/m, corresponding to an interface temperature  $T^* = 1471$  °C. Figure 5(b) shows a cellular interface obtained for a 20 min. holding with  $G_T^\ell = 3000$  K/m, corresponding to an interface temperature of  $T^* = 1462$  °C. In this case, two interfaces are indicated and correspond to the cell tips / quenched liquid and cell root / solid interfaces.

Figure 5(c) shows a closer view of the interface quenched from  $T^* = 1483$  °C. At the bottom of the image is the ULA steel that is composed of  $\delta$  phase. In the middle of the image is the interface; surprisingly, a layer of  $\approx 1$   $\mu\text{m}$  composed of  $\gamma$  and  $\alpha'$  martensite that was identified using EBSD. Some of the martensite laths propagate into the quenched liquid which is composed of  $\gamma$ -phase at room temperature and are visible at the top of the image. The microstructure inside the cells visible in Figure 5(b) is presented in Figure 5(d). In the quenched sample, the cells are composed of dissolving  $\delta$ -phase, again in contact with  $\gamma$  and  $\epsilon$  martensite (see Kikuchi patterns in Figures 5(e) and (f), determined with the crystallographic data from [Martin et al. \(2011\)](#)). Ahead of the cells, the quenched liquid is again composed of  $\gamma$ -phase.

The occurrence of martensite does not seem to be related to the interface morphology (this will be discuss in Section 4.4), but rather to the interface temperature. The high temperature phases at the interface can be deduced from the room temperature microstructures. Nucleation and growth of  $\alpha'$  or  $\epsilon$  martensite is only effective from the  $\gamma$ -phase, meaning that martensite containing interfaces are quenched  $\gamma$  / liquid interfaces. A summary of these results is given in Table 2. From this table, it can be seen that except for holding times of 0 and 1 minute all the interfaces were  $\gamma$  / liquid interfaces leading to  $\alpha'$  or  $\epsilon$  martensite at room temperature.

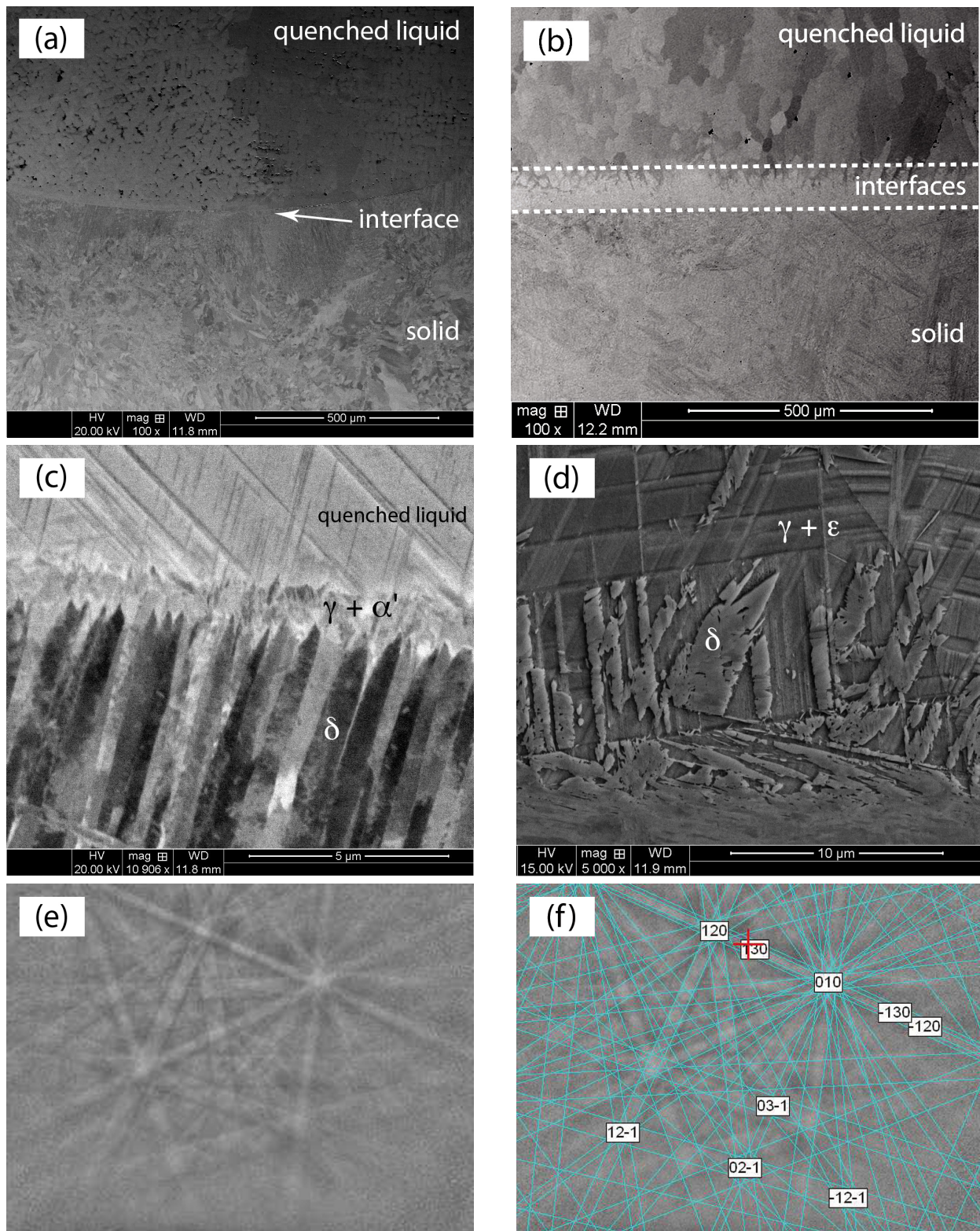


Figure 5: SEM-BSE image of the interface after (a) 10 minute hold with low thermal gradient ( $T^* = 1471^\circ\text{C}$ ), (b) 20 minute hold with low thermal gradient ( $T^* = 1462^\circ\text{C}$ ), (c) 3 minute hold with high thermal gradient ( $T^* = 1483^\circ\text{C}$ ), (d) is an enlarged view of the interface of (b). (e) shows the un-indexed and (f) indexed Kikuchi pattern of  $\epsilon$ -martensite from (d).

Holding time (min.)	$G_T^l$ (K/m)	T* (°C)	interface morphology	solid / liquid interface
0	8000	1500	Planar	$\delta / \ell$
1		1496	Planar	$\delta / \ell$
3		1483	Planar	$\gamma / \ell$
6		1460	Cells	$\gamma / \ell$
0	3000	1500	Planar	$\delta / \ell$
10		1471	Planar	$\gamma / \ell$
20		1462	Cells	$\gamma / \ell$

Table 2: Interface temperature, morphology and nature of the interface for the different samples investigated.

### 4.3. Phases selection

In the Fe-Mn-C system, the  $\delta$  to  $\gamma$  phase transition occurs *via* a peritectic phase transition, in the temperature range of 1494 °C (binary Fe-C system) to 1473 °C (binary Fe-Mn system). This means that the temperature of the interface will govern the presence of  $\alpha'$  or  $\epsilon$ -martensite, but not only because the diffusion of carbon and manganese impose the interface compositions. While in binary systems this operating point is given at a certain temperature, in ternary or higher order systems the additional elements give more degrees of freedom. At a fixed temperature many equilibria are thermodynamically possible even in ternary systems, it is therefore necessary to account for the dissolution path to determine the operating point at the interface.

This has been done by measuring the Mn concentration at the interfaces of the samples. Only Mn was measured since EDX was used and low C amounts cannot be quantitatively measured with this method. Due to the very thin interface thickness compared to the electron probe size, it has to be mentioned that these measurements are approximate but gives a relatively good results due to the large composition differences in Mn between the solid and liquid phases. The results are presented in Figure 6(a-c) for the samples processed with  $G_T^l = 8000 \text{ K.m}^{-1}$ , superimposed with calculated isothermal sections of the Fe-Mn-C phase diagram. In these figures, since carbon was not measured, the manganese compositions were placed on the two-phase domain equilibrium lines corresponding to the phase where the measurements were done. The calculated tie-lines (red lines in Figure 6(a-c)) which were closest to these measurements were added to the isothermal sections. Again, the interface thickness being in the order of nanometers results in quite a high uncertainty on these measurements, however assuming the thermodynamic description of the Fe-Mn-C system is accurate for the tie-line calculations, the analysis presented here is reasonably reliable.

As mentioned earlier, at a given temperature a solid and liquid in contact with large composition heterogeneity want to reach local equilibrium at the interface. In binary systems, having two phases and imposing temperature leaves no degree of freedom and the interfacial compositions are given by the limits of the two-phase domain. The same scheme in a ternary system gives one more degree of freedom, and the thermodynamically possible interfacial compositions are given by the whole frontier of the two phase domain (grey areas in Figure 6(a-c)) as long as the solid and liquid compositions respect a local thermodynamic equilibrium, i.e. are connected by a tie line. The actual interfacial composition will then be imposed by the individual flux of solute through this interface.

The diffusion coefficients for C and Mn in ferrite, austenite and liquid phases were calculated at 1500°C from data found in literature Tekko-no Gyoko (1977); Morgan and Kitchener (1954); Calderon et al. (1971), and are given in Table 3. At 1500°C, the solid / liquid interface is a ferrite / liquid interface. Table 3 shows that while the diffusion coefficients in the liquid phase are similar for Mn and C, in the  $\delta$  phase the carbon diffusion coefficient is higher by two orders of magnitude compared to Mn, and with a value close to that of the liquid phase. This means carbon will govern the interface balance at this temperature and the solid / liquid equilibrium will be close to the Fe-C region of the phase diagram, as confirmed by the measurements at 1496°C presented in Figure 6(a).

Dissolution along the thermal gradient leads to a decrease in the interface temperature of the Fe-C side of the system, leading to the transition from a  $\delta$  / liquid interface to a  $\gamma$  / liquid interface at high temperature which takes place quickly after the experiment begins. In the  $\gamma$  phase, the diffusion coefficients for C and Mn are much smaller compared to their values in the  $\delta$  phase. Moreover it can be observed in Figure 6(b) that at 1483 °C (and from 1490 °C from the thermodynamic calculations) there is a carbon content on the liquidus line that is equal to the average

carbon composition in the liquid. Consequently, the chemical gradient of carbon in the liquid decreases, leading to a decrease in the carbon diffusion flux and a transition from a carbon diffusion driven dissolution to a manganese driven dissolution. This transition is even more pronounced at lower temperature (Figure 6(c)), where it can be seen that at this late stage of the dissolution, the interfacial equilibrium is on the Fe-Mn rich side of the system.

The consequences of this on subsequent phase transformation can be seen in Figure 6(d) where the  $\gamma$  compositions at the interface have been plotted on the Schumann diagram for Fe-Mn-C steels Schumann (1972). In the present work, no  $\alpha'$  martensite was observed at an interface temperature of 1460 °C, but the Schumann diagram is built from austenitization and quenching from 950 °C that is very different from the experimental conditions used here. Two observations arise from this figure. First,  $\gamma$  will transform into martensite upon cooling for all the interfacial compositions reported here. Then, the occurrence of  $\epsilon$  martensite will occur when  $w_{Mn}^{\gamma*} \geq 0.1$  which corresponds to interfacial temperatures below 1473 °C from thermodynamic calculations.

The occurrence of  $\epsilon$  martensite is also related to the existence of a Mn-rich layer in the solid phase, i.e. diffusion

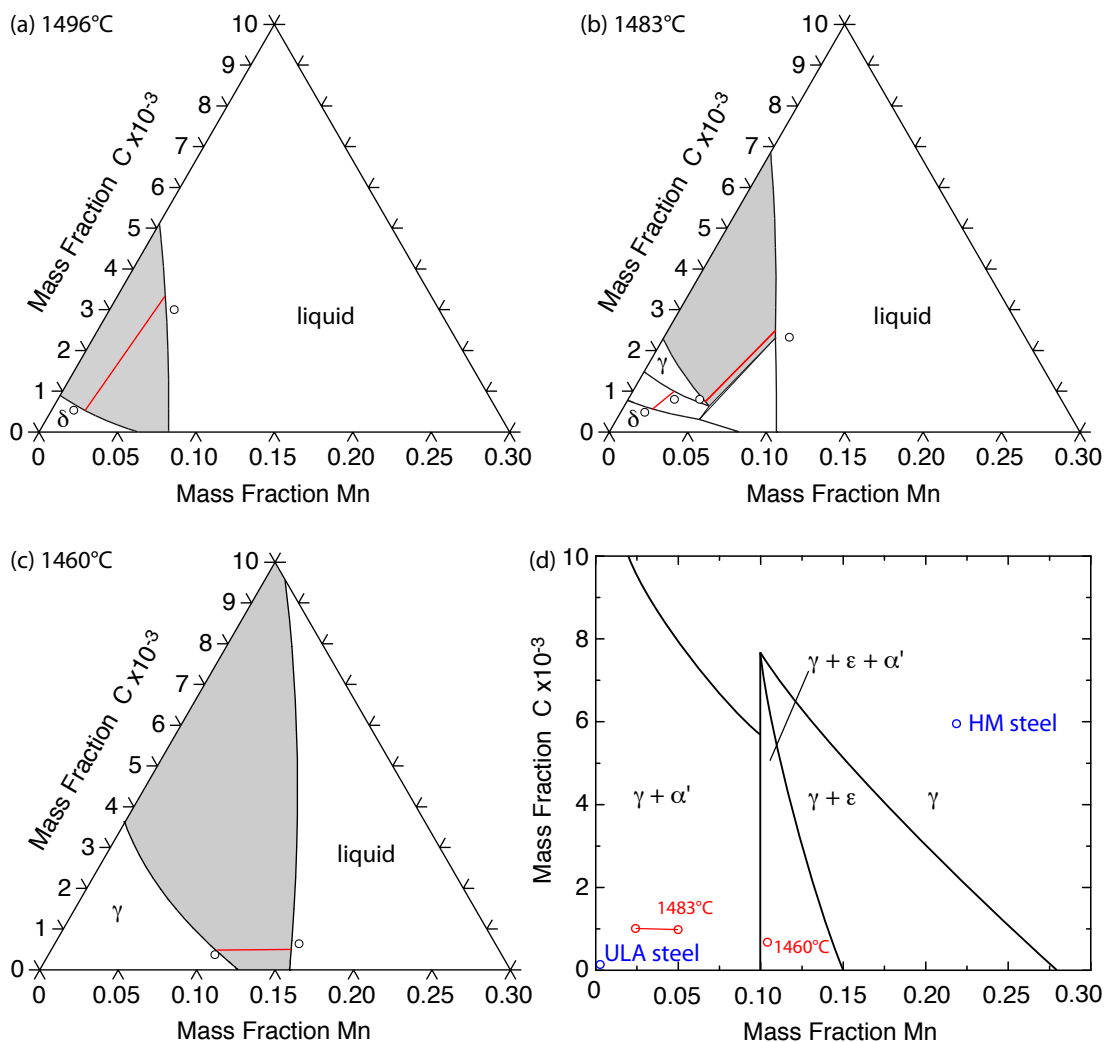


Figure 6: (a-c) Isothermal sections of the Fe-Mn-C system at the temperatures of interest for the samples processed with  $G_T^\ell = 8000 \text{ K}\cdot\text{m}^{-1}$ . The grey areas indicate the interface solid / liquid phases equilibrium, the open circles are the measured interface compositions; calculated tie-lines are also indicated (red lines). (d) Schumann diagram for Fe-Mn-C steels. The austenite compositions presented on (a-c) are indicated together with the nominal composition the ULA and HM steel.

of Mn in the solid phase. From Eq. 6 this condition is  $\Omega_{\text{Mn}}^\varphi > 0$  and can be rewritten as:

$$\Omega_{\text{Mn}}^\varphi = v^* \sqrt{\frac{6 \cdot t}{D_{\text{Mn}}^\varphi}} - \Omega_{\text{Mn}}^\ell \cdot \sqrt{\frac{D_{\text{Mn}}^\ell}{D_{\text{Mn}}^\varphi}} \quad (7)$$

Considering the diffusion length in the solid, the diffusion rate in the solid is given by the derivative of eq. 4 and is equal to  $v_D = \sqrt{3 \cdot D_i^\varphi / 2t}$ . Eq.7 can then be written in dimensionless quantities and becomes:

$$\Omega_{\text{Mn}}^\varphi = \frac{3 \cdot v^*}{v_D} - \Omega_{\text{Mn}}^\ell \cdot \sqrt{\frac{D_{\text{Mn}}^\ell}{D_{\text{Mn}}^\varphi}} > 0 \quad (8)$$

$v^*$  can be imposed either by carbon or manganese diffusion fluxes as discussed previously in this section. The first term of the inequality depends only on the diffusion rate in the solid phase and the second also accounts for alloy composition and thermodynamic equilibrium at the interface (which is temperature dependant).  $\Omega_{\text{Mn}}^\varphi$  was calculated vs. interface velocity for various  $\Omega_{\text{Mn}}^\ell$  values ranging from -1 to -20 for the  $\delta$  and  $\gamma$  phases, together with the ratio  $v^*/v_D$  for each phase. The results are presented in Figure 7. In the model, melting results in a negative value of  $v^*$ ;  $|v^*|$  is plotted in the figure. The values obtained experimentally are also reported; supersaturations were determined from Mn measured compositions (Figure 6(a)-(c)) and the interface velocity is taken as an average velocity determined by the thickness dissolved during the experiment.

The  $v^*/v_D$  curves indicate the limit below which the interface moves faster than the Mn atoms can diffuse in the solid phase so that for values of  $\Omega_{\text{Mn}}^\varphi$  being lower, diffusion in the solid phase can be neglected. Concerning the  $\delta$  / liquid interface, this is the case for high Mn supersaturation in the liquid, which corresponds to the interface temperature of 1496 °C which is in agreement with observations. It can be seen in the figure that diffusion of Mn in ferrite is possible with smaller Mn supersaturations in the liquid phase. Concerning the  $\gamma$  phase, it can be seen that for all the liquid supersaturations,  $\Omega_{\text{Mn}}^\varphi \geq v^*/v_D$  meaning that Mn diffusion in the solid occurs in all cases.

This shows that as soon as the interface temperature is lower than the peritectic temperature, the solid interface is composed of  $\gamma$  phase that will form Mn rich layer of  $\alpha'$  or  $\epsilon$ -martensite upon cooling. Regarding the large difference in

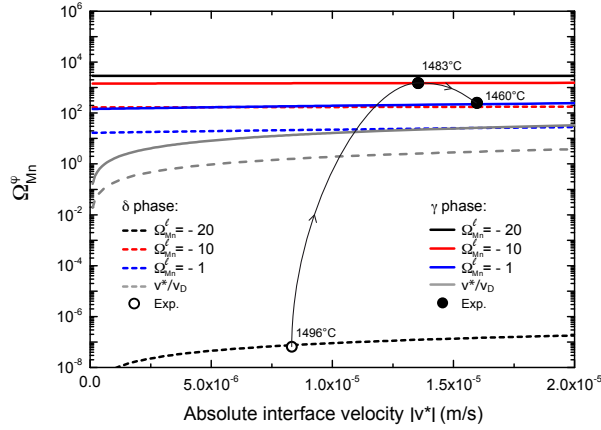


Figure 7: Evolution of  $\Omega_{\text{Mn}}^\varphi$  with interface velocity for  $\Omega_{\text{Mn}}^\ell$  values of -1, -10 and -20. The ratio between interface velocity and diffusion velocity  $v^*/v_D$  is also indicated. The circles indicate determination from experimental values at selected temperatures.

Element	Diffusion coefficients (m <sup>2</sup> /s)		
	$\delta$	$\gamma$	liquid
C	$5.08 \cdot 10^{-9}$	$8.25 \cdot 10^{-10}$	$7.1 \cdot 10^{-9}$
Mn	$1.85 \cdot 10^{-11}$	$2.47 \cdot 10^{-13}$	$5.1 \cdot 10^{-9}$

Table 3: Diffusion coefficients for carbon and manganese in different phases. Values are given for a temperature of 1500 °C and taken from ref. Tekko-no Gyoko (1977) for solid phases, ref. Morgan and Kitchener (1954) for C in liquid and ref. Calderon et al. (1971) for Mn in liquid.

liquidus temperature between the ULA and HM steels (1538°C and 1425°C respectively),  $\gamma$  is the stable solid phase at the interface over a broad temperature range. At the scale of the RSW process, the occurrence of martensite seems unavoidable where the solid / liquid interface temperature is the lowest, e.g. at the edge of the axis of current flow in the melted zone. This explains the fracture position shown in the figure 1 together with the occurrence of the cellular microstructure in this area, which maximises the specific interface between solid and liquid phase. The morphological aspects are discussed in the next section.

#### 4.4. Morphology of the interface

A destabilisation of the interface and the occurrence of cells on the samples quenched from the lowest interface temperatures, e.g. 1462 and 1460 °C was observed. These cellular patterns have also been observed on the RSW samples, as illustrated in Figure 3(d). The cellular spacing is much finer in the RSW process than in the experiments, while the interface velocities are small in both case. No correlation between the solid phase grain size and cellular spacing was observed. The cellular spacing is more likely determined by the diffusion time or the thermal gradient, which differ significantly between the RSW process and the experiments. Understanding the occurrence of the cellular pattern is important, since the cellular array increases the solid/liquid interface surface and thus increases the area of solid containing  $\epsilon$ - martensite that is detrimental to mechanical properties, as shown in Figure 4.

Stability analysis of the planar melting interface has been performed by Chen and Jackson [Chen and Jackson \(1971\)](#) on the same basis as Woodruff [Woodruff \(1968\)](#) but including kinetic undercooling. Both analyses derived from the stability analysis by Mullins and Sekerka [Mullins and Sekerka \(1964\)](#) which has been intensively used for the stability of a solidifying interface. This stability analysis was validated using directional melting of transparent organic alloys [Chen and Jackson \(1971\)](#) and Pb-Sb alloys [Verhoeven and Gibson \(1971\)](#). The latter model is devoted to constrained growth. The stability analysis of growth or dissolution under a purely diffusive regime have been studied by Langer and Turski [Langer and Turski \(1977\)](#) with a stationary symmetric model on a system exhibiting a Mullins-Sekerka instability [Mullins and Sekerka \(1963\)](#). The authors conclude that the cellular configurations are unstable and predict a direct transition from planar to chaotic behaviour. Moreover, this model does not account for the thermal gradient which stabilises the planar interface. Since in the present experiments as well as in the RSW processes the melting velocities are expected to be similar, the high thermal gradient in RSW should therefore stabilise a planar interface compared to the experiments. However a similar cellular array has been observed in both cases, leading to the conclusion that the formation of cells has a different origin.

EPMA measurements were performed on the sample quenched with an interface temperature of 1471 °C because it still exhibited a planar interface but with an interface temperature close to the samples showing a cellular microstructure (1460 and 1462 °C). The results are plotted in Figure 8 on a calculated isothermal section of the Fe-Mn-C system at 1471 °C. The large scatter of the data points in the liquid area are due to the segregations developed throughout the solidification of the liquid during the quench. The compositions of the  $\gamma$  and liquid phases at the interface are estimated by the tie-line shown on the figure, showing good agreement between experiments and calculations. The left side data points show the evolution of the carbon and manganese compositions toward the ULA steel composition. The distance between the solid/liquid interface and the end of the diffusion profile of Mn is 25  $\mu\text{m}$  i.e. a difference of 0.075 °C between these two points. This allows us to consider the assumption of plotting this data on a single isothermal section as relevant.

From Figure 8 it can be seen that the carbon content increases when moving away from the interface to the solid  $\gamma$  phase, before decreasing in the  $\delta$  phase. Obviously carbon diffuses much faster than manganese in the  $\gamma$  phase, but is somehow stopped by the presence of  $\delta$  in the temperature gradient where the C solubility in  $\delta$  is rather limited. The fact that there is a concentration gradient between the solid and liquid phases induces diffusion of C and Mn, but the carbon cannot diffuse easily in the  $\delta$  phase, which leads to an enrichment of  $\gamma$  at the  $\delta/\gamma$  interface. As can be seen in Figure 6 the increase of carbon content may be enough to reach the  $\gamma$  solidus line and enter the ( $\gamma$  + liquid) two phases domain. It would consequently lead to the nucleation of liquid tens of microns from the interface. The carbon concentration profile follows closely the  $\gamma$  solidus line, so that the liquid phase can possibly nucleate along the Mn diffusion layer. This is expected to be the origin of the cellular array observed in both experiment and RSW process via a temperature-gradient zone melting phenomenon (TGZM) [Tiller \(1963\)](#).

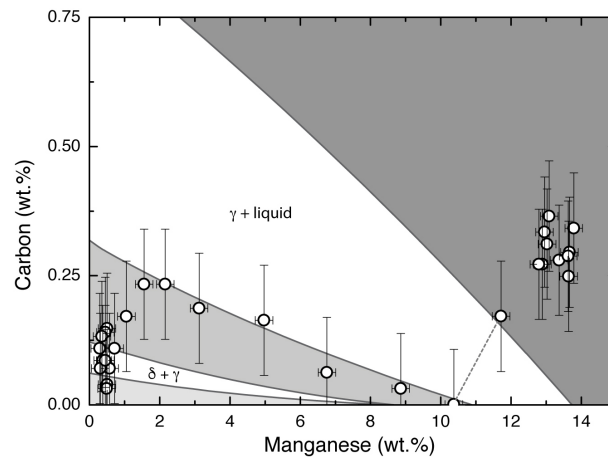


Figure 8: Carbon and manganese concentrations measured by EPMA in the sample held 10 min with  $G_T^\ell = 3000 \text{ K}\cdot\text{m}^{-1}$ , superimposed with the calculated isothermal section at  $1471 \text{ }^\circ\text{C}$ . The dotted line indicates the measured tie-line.

## 5. Conclusions

- A novel experiment has been designed and successfully reproduced the microstructure observed at the melted zone / base steel interface during resistance spot welding.
- The interfacial microstructure formation in Fe/Fe-Mn-C RSW is due to solute diffusion despite the very fast thermal cycle inherent to the process.
- The  $\epsilon$ -martensite forms at  $\gamma$  / liquid interfaces, and that this equilibrium is strongly related to the interface temperature and to the liquid composition, particularly to the carbon content.
- $\epsilon$ -martensite appears when the temperature is locally below the peritectic temperature and when manganese governs the dissolution, making possible a carbon and manganese enrichment at the interface that will favour the nucleation of  $\epsilon$ -martensite upon fast cooling.
- The cellular patterns form due to a solidus temperature gradient coming from the fast carbon diffusion into the solid phases. The cellular pattern was observed at the lowest interface temperatures, where  $\epsilon$ -martensite is most-likely to appear. The highest specific surface of the solid / liquid interface associated with this microstructure explains the weaknesses of RSW dissimilar steel joints observed.

## Acknowledgements

L.D. would like to thank the Région Lorraine for funding her post-doctoral fellowship through the program referenced AOR-RL-2013.

## References

- Andersson, J., Helander, T., Hoglund, L., Shi, P., Sundman, B., 2002. THERMO-CALC & DICTRA, computational tools for materials science. *Calphad* 26 (2), 273–312.
- Baker, J. C., Cahn, J. W., 1971. *Solidification*. ASM, Metals Park, OH.
- Calderon, F., Sano, N., Matsushi, Y., 1971. Diffusion of manganese and silicon in liquid iron over whole range of composition. *Metall. Trans* 2 (12), 3325–3332.
- Chen, H., Jackson, K., 1971. Stability of a melting interface. *J. Cryst. Growth* 8 (2), 184–190.
- Djurovic, D., Hallstedt, B., von Appen, J., Dronskowski, R., 2011. Thermodynamic assessment of the Fe-Mn-C system. *Calphad* 35 (4), 479–491.
- Hillert, M., 1999. Solute drag, solute trapping and diffusional dissipation of Gibbs energy. *Acta Mater.* 47 (18), 4481–4505, 128th TMS Annual Meeting, SAN DIEGO, CALIFORNIA, FEB 28-MAR 04, 1999.

- Langer, J., Turski, L., 1977. Studies in theory of interfacial stability. 1. Stationary symmetric model. *Acta Metall.* 25 (10), 1113–1119.
- Lesoult, G., 2012. Thermodynamique des Matériaux. Vol. 5 of *Traité des matériaux*. Presses Polytechniques et Universitaires Romandes.
- Li, Y., Lin, Z., Shen, Q., Lai, X., 2011. Numerical Analysis of Transport Phenomena in Resistance Spot Welding Process. *J. Manuf. Sci. Eng.* 133 (3).
- Martin, S., Ullrich, C., Simek, D., Martin, U., Rafaja, D., 2011. Stacking fault model of epsilon-martensite and its DIFFaX implementation. *J. Appl. Crystallogr.* 44 (4), 779–787.
- Morgan, D., Kitchener, J., 1954. Solutions in liquid iron. 3. Diffusion of cobalt and carbon. *Trans. Faraday Soc.* 50 (1), 51–60.
- Mujica, L., Weber, S., Pinto, H., Thomy, C., Vollertsen, F., 2010. Microstructure and mechanical properties of laser-welded joints of TWIP and TRIP steels. *Mater. Sci. Eng. A* 527 (7-8), 2071–2078.
- Mullins, W., Sekerka, R., 1963. Morphological stability of a particle growing by diffusion or heat flow. *J. Appl. Phys.* 34 (2), 323–329.
- Mullins, W., Sekerka, R., 1964. Stability of planar interface during solidification of dilute binary alloy. *J. Appl. Phys.* 35 (2), 444–451.
- Pouranvari, M., Marashi, S., 2013. Critical review of automotive steels spot welding: process, structure and properties. *Sci. Technol. Weld. Joining* 18 (5), 361–403.
- Pouranvari, M., Marashi, S. P. H., 2011. Dissimilar Spot Welds of AISI 304/AISI 1008: Metallurgical and Mechanical Characterization. *Steel Research Int.* 82 (12), 1355–1361.
- Rajinikanth, V., Mukherjee, K., Chowdhury, S. G., Schiebahn, A., Harms, A., Bleck, W., 2013. Mechanical property and microstructure of resistance spot welded twinning induced plasticity-dual phase steels joint. *Sci. Technol. Weld. Joining* 18 (6), 485–491.
- Rossini, M., Spena, P. R., Cortese, L., Matteis, P., Firrao, D., 2015. Investigation on dissimilar laser welding of advanced high strength steel sheets for the automotive industry. *Mater. Sci. Eng. A* 628, 288–296.
- Russo Spena, P., De Maddis, M., Lombardi, F., Rossini, M., 2016. Dissimilar Resistance Spot Welding of Q&P and TWIP Steel Sheets. *Mater. Manuf. Process* 31 (3), 291–299.
- Schumann, V., 1972. Martensitische Umwandlung in austenitischen Mangan-Kohlenstoff-Stählen. *Neue Hütte* 17, 605–609.
- Svoboda, J., Gamsjaeger, E., Fischer, F. D., Liu, Y., Kozeschnik, E., 2011. Diffusion processes in a migrating interface: The thick-interface model. *Acta Mater.* 59 (12), 4775–4786.
- Tekko-no Gyoko, S. o. S., 1977. supplement Solidification Comm. of ISIJ. ISIJ, Tokyo.
- Tiller, W., 1963. Migration of a liquid zone through a solid. 1. *J. Appl. Phys.* 34 (9), 2757–2767.
- Verhoeven, J., Gibson, E., 1971. Interface stability of melting solid-liquid interface. 1. Sn-Sb alloys. *J. Cryst. Growth* 11 (1), 29–38.
- Woodruff, D., 1968. Stability of a planar interface during melting of a binary alloys. *Phil. Mag.* 17 (146), 283.